Iceland Liechtenstein Norway grants
"Working together for a green, competitive and inclusive Europe"

GREENCAM for tomorrow

UNIVERSITY OF BUCHAREST
VIRTUTE ET SAPIENTIA

NTNU
Norwegian University of Science and Technology

UNIVERSITATEA DIN BUCUREȘTI
VIRTUTE ET SAPIENTIA

FACULTY OF CHEMISTRY

DEPARTMENT OF ORGANIC CHEMISTRY, BIOCHEMISTRY AND CATALYSIS

MSc Thesis – Report 2

Catalytic amino acid production from biomass-derived intermediates

MASTER: CHEMISTRY OF ADVANCED MATERIALS

STUDENT: MARA ALEXANDRA BADEA

SCIENTIFIC COORDINATOR: Prof. Dr. Simona-Margareta Coman

February 22, 2022

Disclaimer: This was realised with the EEA Financial Mechanism 2014-2021 financial support. Its content (text, photos, videos) does not reflect the official opinion of the Programme Operator, the National Contact Point and the Financial Mechanism Office. Responsibility for the information and views expressed therein lies entirely with the author(s).

CONTENT

Introduction

The CNT application in heterogeneous catalysis is based on their specific important characteristics such as: (i) resistance to acid/basic media, (ii) possibility to control, up to certain limits, the porosity and surface chemistry and (iii) easy recovery of precious metals by support burning resulting in a low environmental impact [1]. The combination of these properties makes CNT attractive and competitive catalyst supports by comparison with activated carbons. However, in the case of as-produced CNT it has to be noticed that such a material does not possess an high amount of functional groups on it's surface and mainly surface defects can be considered as anchoring sites for metals. In order to evaluate the role of surface defects on the final metal dispersion, the interaction between iron, cobalt or nickel and MWCNT, SWCNT, activated carbon or layered graphite has been studied [2]. On SWCNT and layered graphite, no coating was observed due to the low density of surface defects. However, for MWCNT and activated carbon, a better wetting has been achieved and, in the case of iron on MWCNT, a particle size of 5–15 nm has been measured. Several other metals were deposited on MWCNT by using the wetness impregnation technique. For instance, palladium, platinum, gold and silver particles obtained presented a mean size of 7, 8, 8 and 17 nm, respectively, and were mostly found on the outer surface of the CNT [3].

On the other hand, magnetic nanoparticles (MNPs) have been gaining increasing interest in the last years due to their valuable properties such as high surface area, low toxicity and super-paramagnetic behavior [4]. This intrinsic property may allow an easier separation from reaction mixtures by the use of an external magnetic field. In addition, the presence of a large number of hydroxyl groups on the external surface affords both the deposition of inorganic shells containing different catalytic active phases or the direct immobilization of a variety of catalytic functionalities *via* covalent bonds [5]. In this context, not long ago an efficient Ru(4wt%)@MNP-SiO_2 catalyst for the oxidation of levulinic acid (LA) to succinic acid (SA) (S_{SA} = 96-98% for X_{LA} = 59-79%) was reported [6].

Amino acids are valuable products for industry due to their versatility, glutamic acid, lysine, methionine and threonine covering more than 95% of the total market volume [7]. This is why the researchers focus now in developing on two directions: the discovery of new production methods regarding this four amino acids and the discovery of production methods regarding the rest of amino acids. Today, amino acids are primarily manufactured *via* microbial cultivation processes, which are costly, are time consuming, and require extensive separations processes. The development of efficient chemical methods to convert abundant and renewable feedstocks into

amino acids is, therefore, highly attractive but it have been largely unsuccessful to date. As an alternative, chemocatalytic approaches to produce amino acids from renewable feedstocks such as bio-based sugars could offer a rapid and potentially more efficient means of amino acid synthesis, but efforts to date have been limited by the development of facile chemistry and associated catalyst materials to selectively produce α-amino acids.

In our knowledge, only one recent report on a heterogeneous catalyst that directly transforms lignocellulosic biomass-derived α-hydroxyl acids into α-amino acids, including alanine, leucine, valine, aspartic acid, and phenylalanine in high yields exist in literature [8]. In this work the authors showed that ruthenium nanoparticles supported on carbon nanotubes (Ru/CNT) exhibit exceptional efficiency compared with catalysts based on other metals, due to the unique, reversible enhancement effect of NH_3 on Ru in dehydrogenation.

Objectives

The aim of this work was to develop efficient heterogeneous catalysts able to directly transform lignocellulosic biomass-derived lactic acid into alanine. For this a series of Ru-based heterogeneous catalysts with (1) as-received MWCNT and (2) magnetic nanoparticles (MNPs) carriers were prepared and characterised.

(1) Ru/CNT catalysts, with 1wt%, 3wt% and 5wt%Ru, respectively were synthesized and characterised. As we already specified in the introduction, literature study indicates that ruthenium nanoparticles supported on carbon nanotubes (Ru/CNT) exhibit exceptional efficiency compared with catalysts based on other metals, due to the unique, reversible enhancement effect of NH_3 on Ru in dehydrogenation. However, in their study, the authors used only a catalyst with 3wt%Ru, prepared by impregnation of the as-received CNT. Much more attention must be paid to the concentration of ruthenium which can lead to ruthenium particles with varying degrees of dispersion and oxidation, these characteristics being able to decisively influence the course of the reaction in which they are applied.

(2) To overcome the catalysts separation issue, the use of magnetic nanoparticles emerge as a viable solution; their insoluble and paramagnetic nature enables their easy and efficient separation from the reaction mixture with an external magnet. That is why, a second kind of Ru-based catalysts used as carrier magnetic nanoparticles (MNP) for the synthesis of cationic Ru(III)/functionalized silica coated magnetite nanoparticles.

Experimental part

All the chemicals and reagents were of analytical purity grade, purchased from Sigma-Aldrich and used without further purification. All the chemicals and reagents were of analytical purity grade, purchased from Sigma-Aldrich and used without further purification. Two kind of multi-walled carbon nanotubes (MWCNTs) were purchased from Sigma-Aldrich with the following features: (1) preparation method Catalytic Chemical Vapor Deposition (CVD) (CoMoCAT®), over 95% carbon, O.D×L/6-9 nm × 5 μm and armchair configuration, and (2) preparation method Catalytic Chemical Vapor Deposition, over 90% carbon basis, D×L/110-170 nm × 5-9 μm and armchair configuration. Hydrated ruthenium chloride ($RuCl_3xH_2O$) had ~37% Ru basis. PTFE membrane filters with 0.45 μm pore size were purchased from Merck.

a) Materials preparation methodologies

a1) Ru supported onto MWCNT (Ru/CNT)

The CNT-supported Ru nanoparticles were prepared by wet impregnation method. Typically, 0.5g CNT (CoMoCAT®) was added into the aqueous solution of $RuCl_3$ (200mg/10 mL H_2O) and then subjected to stirring for 1 h at room temperature. The solution was aged 2 h and after that the water was evaporated at 80°C. The catalyst was calcined at 350°C, in static, for 4 h. The calcination temperature was established based on the TG analysis of CNT carrier (see Annex 1). The solid product was reduced in H_2 gas at 450°C for 2 h. The metal loadings were ~1 wt %, ~3 wt % and ~5 wt % and the obtained samples were denoted 1%Ru/CNT, 3%Ru/CNT and 5%Ru/CNT.

a2) Ruthenium based magnetic nanoparticles

The two steps preparation followed a literature reported procedure [9]:

(i) the synthesis of the magnetic carrier that is comprised of spherically amino functionalized silica-coated Fe_3O_4 nanoparticles. In a typical procedure, 7 g of sodium dodecylbenzenesulfonate (technical grade, purchased from Acros Organics) was added in 60 mL dried xylene (purchased from Aldrich) and ultrasounded for 20 minutes, then stirred in an oil bath at room temperature. The air was removed from the reaction vessel by purging it with nitrogen. 3.23 g (8.0 mmoles) iron (III) nitrate nonahydrate and 0.8 g (0.4 mmoles) iron (II) chloride tetrahydrate were dissolved in 3.6 mL deionized water purged with nitrogen and added to the mixture of xylene and surfactant. The obtained mixture was stirred overnight under inert atmosphere at room

temperature till homogeneization. The emulsion was heated at 90°C, for 1 h, and then 4 mL of hydrazine 35% solution was added and stirred for 3 h, at 90°C and 1 h at 40°C, under inert atmosphere. Afterwards a mixture of 3 mL tetraethylortosilicate (TEOS, purchased from Aldrich) and 3 mL 3-aminopropyltriethoxysilane (purchased from Aldrich) was added and the emulsion was stirred overnight in air atmosphere. The obtained black solution was transferred in a Berzelius flask and the obtained particles were separated with the aid of a Fe-Nd-B magnet. The separated particles were then washed five times with ethanol, recovered with a magnet, washed again with acetone and dried under vacuum.

(ii) the impregnation of the magnetic nanoparticles carrier with $RuCl_3$ solution in basic medium as follow: 2 g of Fe_3O_4–SiO_2/NH_2 were added to 200 mg $RuCl_3$ aqueous ruthenium (III) chloride (purchased from Aldrich) dissolved in 400 mL distilled water. The pH was adjusted at 13 with the aid of a NaOH aqueous solution (1M). The mixture was kept under stirring at 25 °C for 24 h. The solid was then magnetically collected from the solution, washed twice with distilled water and acetone and dried in vacuum.

b) Characterization techniques

Prepared samples were characterized by adsorption-desorption isotherms of liquid nitrogen at -196 °C, X-ray diffraction (XRD), temperature programmed desorption of H_2 and NH_3 (H_2-TPD and NH_3-TPD), IR diffuse reflectance with Fourier transform (DRIFT), Raman spectroscopy and thermogravimetric-differential thermal analysis (TG-DTA).

Textural characteristics (surface area, pore volume and pore diameter) were determined from the adsorption-desorption isotherms of nitrogen at -196 °C using a Micromeritics ASAP 2020 Surface Area and Porosity Analyzer.

Powder X-ray Diffraction patterns were collected at room temperature using a Shimadzu XRD-7000 apparatus with the Cu Kα monochromatic radiation of 1.5406 Å, 40 kV, 40 mA at a scanning rate of 1.0 2θ min^{-1}, in the 2θ range of 10^o–90^o.

Hydrogen chemisorption and NH_3-temperature programmed desorption (NH_3-TPD) were recorded using a Micromeritics apparatus – Autochem II (Chemisorption Analyzer). Approximately 20 mg freshly reduced Ru/CNT was heated at 650°C under N_2 for 0.5 h to remove the hydrogen adsorbed on Ru atoms. After that, the temperature was reduced to 150°C and waited until baseline became stable. Subsequently, successive doses of H_2 gas were provided. The measurements for NH_3-TPD were performed in the same manner.

DRIFT spectra were recorded with a Thermo 4700 spectrometer (400 scans with a resolution of 4 cm^{-1}) in the range of 400–4000 cm^{-1}.

TG-DTA analyses were recorded using a Shimadzu apparatus in a Pt crucible. The heating rate was of 10°C min^{-1}, respectively, starting from room temperature till 850 °C under a nitrogen flow of 50 mL min^{-1}.

Results and discussions

Ru/CNT samples characterisation

Liquid nitrogen adsorption-desorption isotherms at -196°C

Figures 1-3 show the nitrogen adsorption-desorption isotherms at -196 °C and the corresponding pore size distribution obtained through the Barret–Joyner–Halenda (BJH) method for the 1%, 3% and 5%Ru/CNT samples.

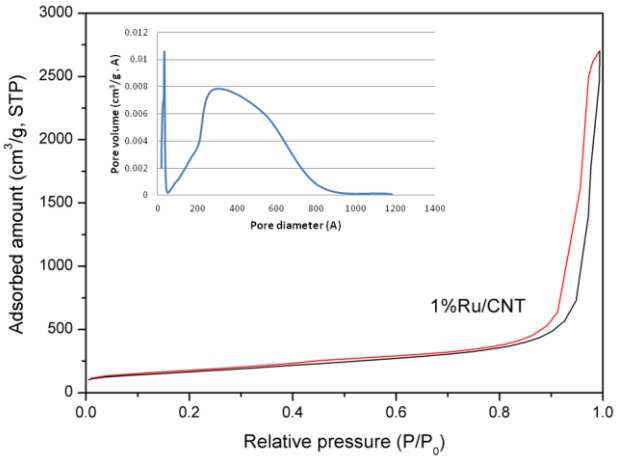

Figure 1. Nitrogen adsorption-desorption isotherm and pore size distributions (inset) for 1%Ru/CNT sample

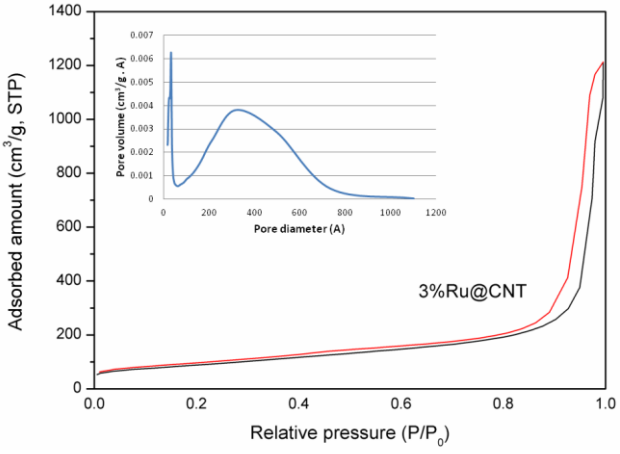

Figure 2. Nitrogen adsorption-desorption isotherm and pore size distributions (inset) for 3%Ru/CNT sample

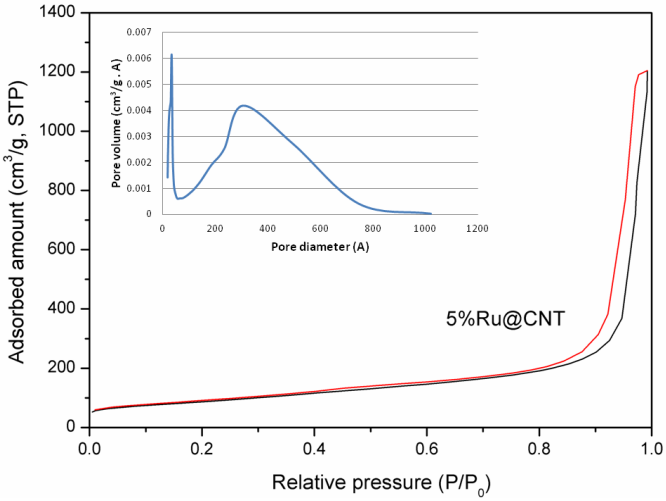

Figure 3. Nitrogen adsorption-desorption isotherm and pore size distributions (inset) for 5%Ru/CNT sample

The pore structure parameters of Ru/CNT sample determined by BET, t-plot and BJH methods are summarized in Table 1. The specific surface area (S_{BET}), the total pore volume (V_p) and the porosity of the samples are presented in Table 2. The specific surface area (S_{BET}) of the samples was calculated following the BET (Brunauer–Emmett–Teller) procedure with eight relative pressures (p/p_0) of nitrogen in the range of 0.07–0.2. The t-plot method was used to determine the micropore and external surface area and also the micropore volume. The Barret–Joyner–Halenda (BJH) method was used to determine pore size distribution, considering the desorption curves.

Table 1. The pore structure parameters of Ru/CNT sample determined by BET, t-plot and BJH methods

Entry	Sample	S_{BET} (m^2/g)	Micropore surface area (m^2/g)	External surface area (m^2/g)	Total pore volume (cm^3/g)	Micropore volume (cm^3/g)	Mezopores volume (cm^3/g)	Avarage pore size (BJH, nm)
1	1%Ru	584	56	527	3.82	0.02	3.80	3.3 and 27.7
2	3%Ru	315	22	293	1.67	0.01	1.66	3.3 and 31.9
3	5%Ru	310	20	291	1.88	0.01	1.87	3.3 and 30.5

All the nitrogen adsorption-desorption isotherms (Figures 1-3) can be divided in four parts as shown in Figure 4, indicating a multistage adsorption process.

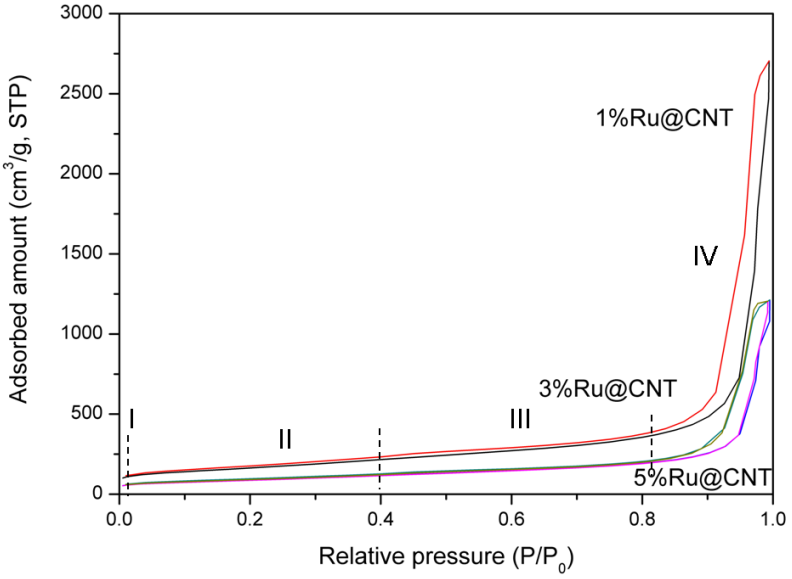

Figure 4. Nitrogen adsorption-desorption isotherms of Ru/CNT samples

In part I (around p/p_0 of 0.01), the isotherm is normally of type I characteristic indicated by the fact that the nitrogen adsorption amount increases at ultra-low pressure. Such a process occurs in pores with molecular size, suggesting that in the samples there are micropores contributed by the opened inner cavities in the CNT with very small diameter. Nitrogen molecules, whose diameter is about 0.364 nm, can fill in these pores under ultra-low adsorption pressure. However, as Figure 4 shows, in the case of our samples, there is only a very slightly increased amount of nitrogen adsorption in this portion of isotherms. Table 1 shows both very low micropores surface area and micropores volume. Part II of the isotherms (p/p_0 = 0.01-0.40) shows a slowly increases of the nitrogen adsorption amount with the formation of the surface monolayer.

A hysteresis loop is clearly visible in part III and IV of the isotherm, associated with the capillary condensation in mesopores [10]. These ranges show Type IV isotherm characteristics. Part III corresponds to capillary condensation occurring at medium relative pressure range (p/p_0 = 0.4-0.85) in small mesopores with a size of 3.3 nm (Table 1, column 9), which is similar to the inner cavity diameter of the pristine opened CNT [11]. As Table 1 shows this size remains constant, irrespective of the ruthenium concentration, indicating a lack of ruthenium deposition during the impregnation process in the inner hollow cavity of the CNT.

When the pressure nears to the saturation pressure (part IV of the isotherm, p/p_0 = 0.85-0.99), the adsorption amount shows a great increase, indicating a strong capillarity in larger mesopores. In multi-well CNTs these hysteresis loop (H3 type) correspond to pore size of about

20-40 nm which is likely to be contributed by aggregated pores since there are not CNT with so large inner cavity diameter and, accordingly, to form so big inner porosity [11]. Therefore, the so-called aggregated pores are formed by the confined space among the isolated nanotubes of different orientation which interact by inter-molecular force creating a relatively stable aggregated structure (Figure 5).

The corresponding pore sizes to aggregated pores in Ru/CNT samples slightly vary in a range of 27.7-31.9 nm (Table 1). This variation, along with the decreases of the external surface area clearly indicates the deposition of the ruthenium take place on the outer side of the CNT tubes. Moreover, the high difference between the S_{BET} of the 1%Ru/CNT sample (Table 1, entry 1) and the S_{BET} of the 3%Ru/CNT and 5%Ru/CNT (Table 1, entries 2 and 3), respectively, indicates a high uniform deposition, with a high dispersion degree, of the ruthenium particles for the 1%Ru/CNT sample and a high agglomeration of the ruthenium particles in the case of the last two samples (Figure 5). These results are in agree with Chu and co-workers which showed not long ago [12] that the main Ru particle size is smaller if ruthenium is deposited on the inner surface of the carbon nanotubes (denoted Ru-in-CNTs) than that of deposited ruthenium on the external surface of the nanotubes (denoted Ru-out-CNTs), indicating that particle sintering is prevented in Ru-in-CNTs under the reduction condition due to the spatial restriction of the CNT channels. The narrower size of the aggregated pores in the case of the 1%Ru/CNT sample also indicates a slightly denser packaging of the CNT network, again confirming the high uniform deposition of the ruthenium particles in the case of this sample.

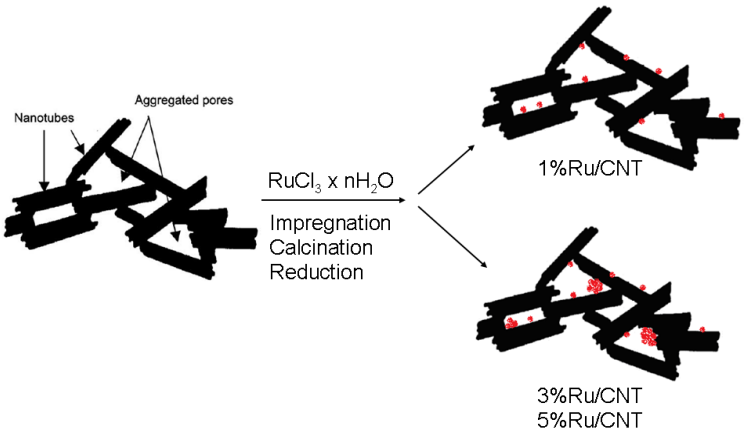

Figure 5. Schematic structural model for the aggregated pores in CNTs adapted from [11] and the structural models of the Ru/CNT samples

The agglomeration of the Ru particles on the outer walls of CNT for high concentrations of ruthenium (i.e., 3% and 5%, respectively) is also confirmed by XRD measurements.

X-Ray diffraction (XRD)

The X-ray diffraction (XRD) patterns of the as-synthesized Ru/CNT powders were recorded to examine their phase purity and crystallinity. As shown in Figure 6, CNT has two characteristic reflection lines at 26° and 43.9°, corresponding to the (002) and (100) facets, respectively, according with literature data [13,14]. The line from 26° indicates that the spacing between the sp^2-C layers in the multi-walls CNTs is 0.343 nm [13]. As the XRD pattern of the CNT carrier shows the impregnation of the CNTs with different quantities of ruthenium salts and the activation steps does not damaged the CNT structure.

In the case of 1%Ru/CNT sample no diffraction lines corresponding to ruthenium particles are evidenced suggesting the formation of nanoparticles with narrow size and high dispersion for this sample (Figure 6, spectrum in black). However, for the samples 3%Ru/CNT and 5%Ru/CNT, apart from the lines characteristic to the CNT carrier, some characteristic lines corresponding to the Ru (hexagonal phase; JCPDS Card No. 06-0663) at 38.3°, 42.8°, 58.4°, 69.6° and 78.7°, assigned to (100), (101), (102), (110) and (103) reflections of metallic Ru are evidenced. [15] This indicates an agglomeration of the ruthenium species during the samples preparation with the formation of larger ruthenium particles.

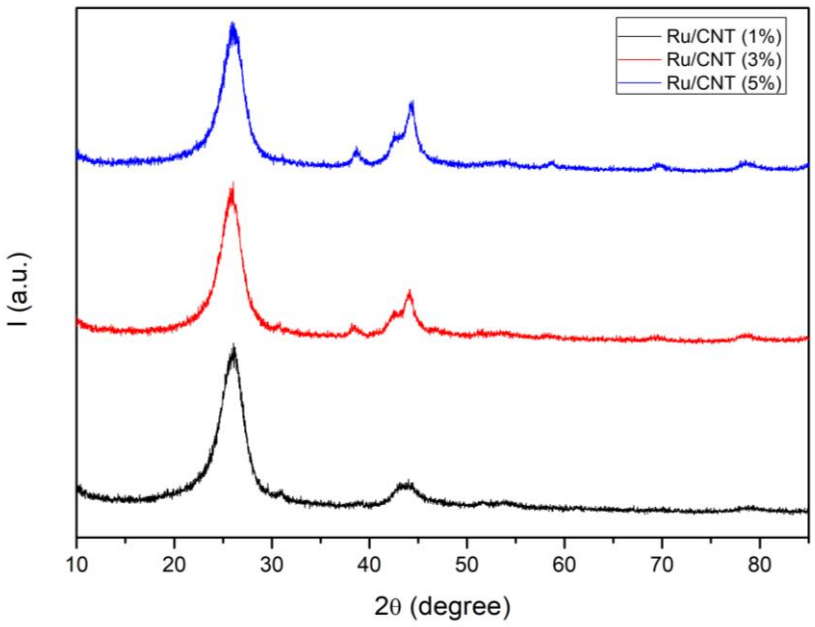

Figure 6. XRD patterns of different Ru-based CNTs catalysts

The average size of ruthenium crystallites was determined from the Debye-Scherrer equation taking the (100) reflection of ruthenium particles [16]:

$$d = \frac{k\lambda}{\beta \cos\theta}$$

Where: d is the crystallite size in nm; k = 0.94; λ is the wavelength of the X-ray (1.54178 Å); θ is the half-diffraction angle and β is the full width at half-maximum (FWHM) in radians for the 2θ value (38.3°).

The ruthenium particle size diameter is 9.0 nm for the 3%Ru/CNT sample and 10.6 nm for the 5%Ru/CNT sample.

NH_3-TPD

Chen et al. [17] reported that the deviation of the CNT graphene layers from planarity causes p-electron density shifting from the concave inner surface to the convex outer surface, leading to an electron deficient internal surface and an electron-enriched external surface. This electron density loss is partially compensated through the interaction with the encapsulated metal [18] which would destabilize the metal nanoparticles and facilitate their reduction. In connection with this statement and with the findings from the previously results obtained from the characterization techniques applied for the elucidation of the structural and chemical characteristics of the Ru/CNT samples, temperature programmed desorption of ammonia (NH_3-TPD) was performed to assess the acid properties of the CNTs support and corresponding Ru-based catalysts. It is well known the oxide form of the noble metals display Lewis acid characteristics. The existence of the Bronsted acidity should also does not be excluded through the possibility of the -OH groups existence, anchored on the oxide particles.

The temperature of maximum desorption rate, i.e., the temperature of a TPD peak, is used as a measure of the acid strength of the sorption sites. The method has the limitation that it can distinguish sites by sorption strength but not Lewis (L) from Bronsted (B) type sites. However, for zeolites there are several literature reports which divide the desorption regions in two, bellow and above 400°C, referring to low-temperature (LT) and high-temperature (HT) regions, respectively [19]. The peaks in the HT region are attributed to the desorption of NH_3 from strong B and L sites while the assignment of the LT peaks is still controversial [19]. The possibility that weak L acid

sites were responsible for the LT peak was considered [20] but the release of NH_3 hydrogen-bound to NH_4^+ cations were also not excluded [21].

The NH_3-TPD profiles of the CNT and Ru/CNT samples are given in Figure 7.

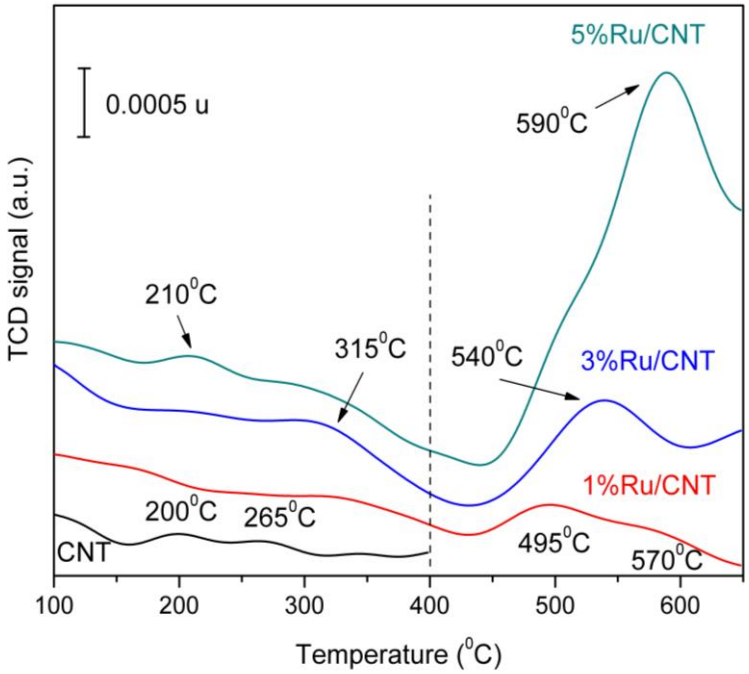

Figure 7. NH_3-TPD profiles for the Ru/CNT samples

As Figure 7 shows, the CNT carrier contains only an insignificant amount of acid sites, situated in the LT region. However, their impregnation with ruthenium salt followed by calcination and reduction leads to the appearance of acid sites, their highest concentration being in the HT region. Moreover, the higher the ruthenium concentration the higher the concentration of the L and B acid sites. Nevertheless, the level of the acid site concentration is very low and vary from around 0.4 μmol/g (1%Ru/CNT) to 2.2 μmol/g (5%Ru/CNT).

As previously shown, the obtained results from the nitrogen adsorption-desorption isotherms and XRD measurements clearly indicate that ruthenium particles are deposited on the external surface of the CNT tubes. However, if in the case of 1%Ru/CNT sample, small ruthenium particles with a high dispersion are formed, for samples with 3% and 5%Ru, the formation of larger particles with a low dispersion is preponderant. In agree with Chen et al. [22] such large particles are hardly reduced. Therefore, the NH_3-TPD new peaks from the TPD profiles of Ru/CNT (Figure 7) could be assigned to a partial reduction of Ru^{3+} to Ru^0 species with the formation of some RuO_x-OH species along side the metallic particles.

H_2-TPD

The effect of reduction temperature on catalytic behavior has been the subject of many investigations. Many studies have shown both reduced catalytic activity and reduced hydrogen chemisorption capacity after reduction in hydrogen at high temperatures (> 500°C) but a clear understanding of the phenomena involved is still lacking. Reduction at high temperatures may result in strongly chemisorbed hydrogen, may cause loss of spillover hydrogen altering the local charge transfer from the support to the metal at the particle boundary, may induce changes in morphology of the metal crystallite and may affect reduction of the support leading to the formation of an alloy with atoms from the support [23].

In this study the temperature-programmed desorption of hydrogen was performed in order to check the strength of metallic ruthenium interactions with hydrogen. Therefore, the H_2-TPD spectra of previously reduced (450°C) Ru/CNT samples were measured. The maximum desorption temperatures and corresponding desorbed amount of hydrogen are given in Table 2.

Table 2. H_2-TPD parameters for Ru/CNT samples and CNT carrier

Entry	Catalyst	H_2 desorbed (mmol/g)	Peak temperature (°C)
1	CNT	1.18	143
2	1%Ru/CNT	0.010	328
		0.008	340
		0.008	370
	Total	**0.026**	
3	3%Ru/CNT	0.003	290
		0.005	310
		0.008	390
		0.004	520
	Total	**0.020**	
4	5%Ru/CNT	0.002	590

The maximum of the hydrogen desorption peak found in this study for CNT carrier is lower than that for graphite (143°C versus 207°C) [24], suggesting a lower binding energy of the hydrogen adsorption in the case of CNT. Many authors claim that hydrogen molecules mostly

adsorb on the outer surfaces of CNT and the reduction in binding energy value is generally attributed to the surface curvature [25].

The hydrogen desorption begins at 200°C for all Ru-based catalysts; however, apparently the maximum desorption peak depends on the ruthenium concentration. For catalysts with 1% and 3%Ru the H_2-TPD profiles comprise three or more peaks (the maximum temperature for these peaks are given in Table 3) owing to the formation of various active sites or to the effect of spillover hydrogen, while for 5%Ru/CNT sample, the only one maximum desorption peak was visible at 590°C. The peaks with the desorption temperature lower than 500°C (1% and 3%Ru) can be attributed to the dissociative adsorbed hydrogen and spillover hydrogen simultaneity, while the peak at above 500°C (3% and 5%Ru) can be associated to the spillover hydrogen stabilized by hydroxyl groups from the ruthenium oxides surface. A low temperature of the hydrogen desorption indicates, therefore, a weaker adsorption of H_2 and its greater mobility on the catalyst surface while a high temperature for the hydrogen desorption indicates a strongly chemisorbed hydrogen [26]. Based on H_2-TPD results, the mobility of hydrogen on the surface of catalysts can be ordered in the following sequence: 1%Ru/CNT > 3%Ru/CNT > 5%Ru/CNT. Moreover, the higher the ruthenium concentration the lower the hydrogen desorbed amount. These data are also in agree with the NH_3-TPD results according to which the higher the amount of ruthenium the lower the reduction degree of the agglomerated ruthenium particles.

DRIFT spectroscopy

It should be noted that the spectrum of the pristine CNT is quite similar to others presented in the literature [27]. Some claimed MWCNT-specific infrared (IR) spectral features include peaks associated with O−H vibrations (1600 and 3740 cm^{-1}), carboxylic groups (1740 cm^{-1}), -C=C- stretching vibration (1523 cm^{-1}) and C−H stretching vibrations (close to 3000 cm^{-1}), even though they correspond to defects and impurities rather than the MWCNT structure itself (Figure 8). The most important use of infrared spectroscopy in MWCNT research is the characterization of surface functionalization [28] and this will be discussed in the next section.

The infrared spectra of the CNT and Ru/CNT samples are given in Figure 8. Similar peaks were identified for all samples. However, in the case of Ru/CNT samples a new peak at 3630 cm^{-1} was identified into the corresponding spectra, associated with possible O-H vibrations from RuO_x-OH groups.

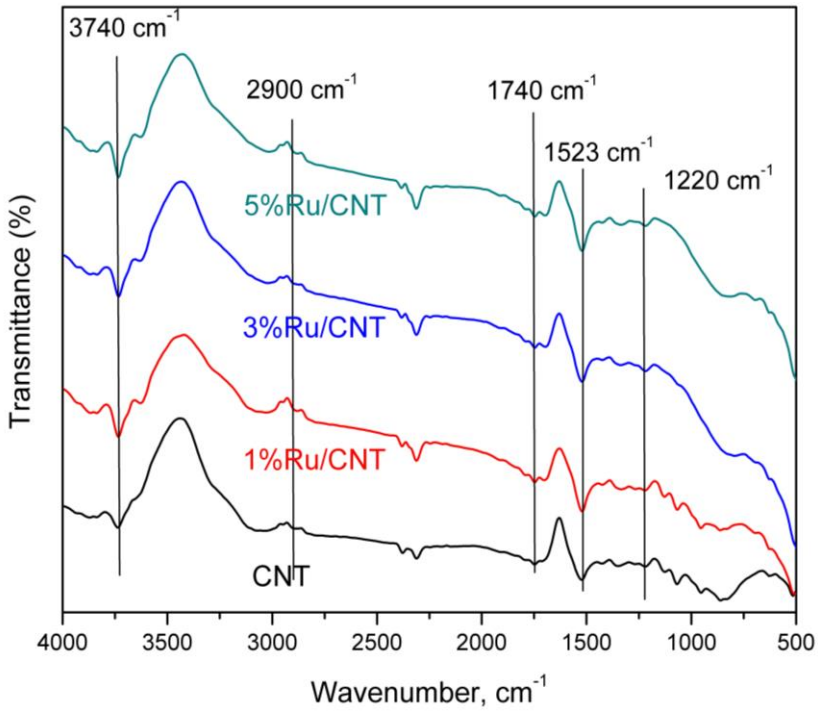

Figure 8. IR spectra of the CNT and Ru/CNT samples

Ruthenium based magnetic nanoparticles carrier

X-Ray diffraction

Magnetite nanoparticles are very sensitive to oxygen, and in the presence of air some might undergo oxidation to maghemite (γ-Fe_2O_3) phase. Since both magnetite (Fe_2O_3) and maghemite (γ-Fe_2O_3) have a spinel structure, their diffraction lines are close and it is difficult to distinguish them from one another by X-ray diffraction pattern. Moreover, depending on pH of the aqueous solution containing Fe^{3+} ions, it is also possible to form goethite, α-FeOOH by hydrolysis or by reaction with OH^- species [29]. The formation of hematite (α-Fe_2O_3) is more difficult than that of the maghemite phase, occurring only under thermal dehydration conditions.

To quantify the proportion of iron oxide, formed in a mixture iron oxide-silica, the XRD diffraction patterns were used. As visible in Figure 9, X-ray diffractogram (XRD) of the as synthesized samples showed a diffraction pattern characteristic of dominant magnetite (Fe_3O_4) phase. In particular, the peaks at 2θ equal to 30.1°, 35.4°, 43.1°, 53.4°, 57.1°, and 62.6° can be indexed as (220), (311), (400), (511), and (440) lattice planes of cubic magnetite, respectively

(JCPDS 19-629). Nevertheless, the sharp diffraction lines indicate the presence of trace amounts of goethite phase probably formed as contaminants during the preparation processes. Finally, the broad diffraction line at around 2θ = 20° is due to the amorphous silica shell on the surface of the magnetite nanoparticles. Very important, no characteristic diffraction lines for ruthenium particles appeared after the magnetite impregnation, indicating a well dispersion of these particles on the surface (Figure 9, spectrum in red).

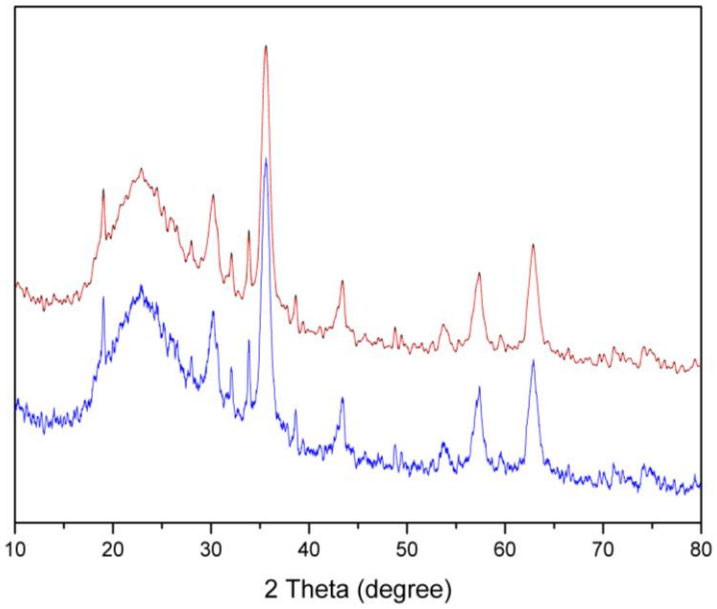

Figure 9. The XRD paterns of Fe_3O_4–SiO_2/NH_2 (blue) and Ru-Fe_3O_4–SiO_2/NH_2 (red) sample

In addition, the crystallite size was calculated through evaluation of the line broadening β and the corresponding Bragg angle θ, by using the Scherrer Equation ($D_{hkl} = 0.9\lambda/\beta\cos\theta$, in which β stands for the half-width of the XRD diffraction line, θ is the peak position in angles, and λ is the CuK_α radiation wavelength, that is 1.54056 Å) [30]. The average Fe_3O_4 crystallite size, calculated by applying the Debye-Scherrer equation to the most intense reflection peak (311), was approximately of 18 nm.

DRIFT spectroscopy

The DRIFT spectrum (Figure 10) confirms the coating of the magnetite surface and the existence of amino groups (–NH_2 bending) on the surface of the particles. The presence of magnetite nanoparticles is signalled by the presence of two strong absorption bands at around 632 and 585 cm^{-1}, resulted from the split of ν1 band at 570 cm^{-1} corresponding to the Fe–O bond of bulk magnetite (not shown in figure) [31].

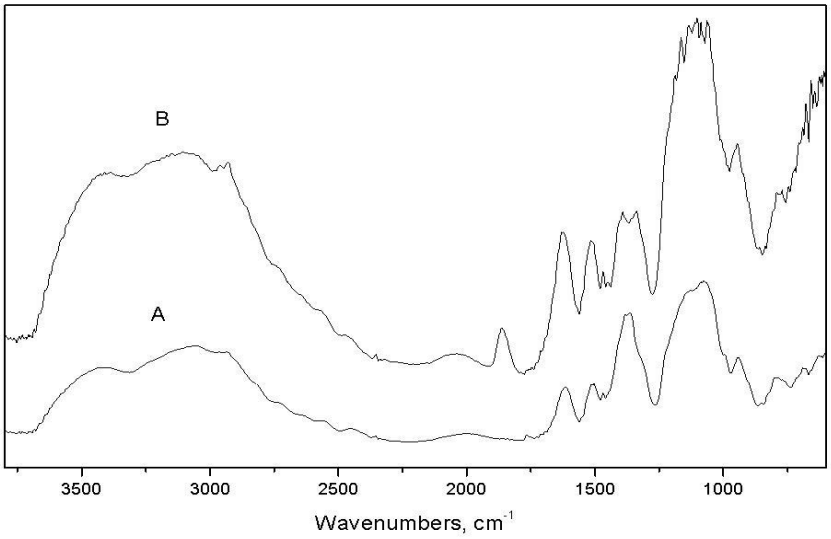

Figure 10. The DRIFT spectra of the Fe_3O_4–SiO_2/NH_2 (spectra A) and Ru-Fe_3O_4–SiO_2/NH_2 (spectra B) sample

The silica network is adsorbed on the magnetite surface by Fe–O–Si bonds which were confirmed by the band at around 584 cm^{-1}. Moreover, the Si-O–H and Si–O–Si groups are present in the IR spectra with bands at 1113, 1048 and 989 cm^{-1}. The absorption bands at 922 and 862 cm^{-1} revealed the presence of Si–O–H stretching and OH vibrations on the surface of magnetite, while the two broad bands at 3417 and 1625 cm-1 can be ascribed to the N–H stretching vibration and NH_2 bending mode of free NH_2 group, respectively [32]. The presence of the anchored propyl group was confirmed by C–H stretching vibrations that appeared at 2930 and 2862 cm^{-1} while the hydrogen-bonded silanols were confirmed by the bands at around 3200 and 3470 cm^{-1} [32].

The deposition of ruthenium species led to a reduction of the intensity bands of both 3417 and 1625 cm^{-1} bands, ascribed to the N–H stretching vibration and NH_2 bending mode of free NH_2 group, in the same time with the appearance of a new band at 1850 cm^{-1} assigned to hydrochloride - C-$NH_3^+Cl^-$ species (Figure 10, spectra B). This band confirms the docking of the $Ru(OH)_xCl_{3-x}$ ruthenium species onto the silica-coated magnetite nanoparticles.

Not less important, the obtained catalyst still preserves its magnetic properties, the separation from the aqueous solution being easily done with the aid of an external magnet (Figure 11).

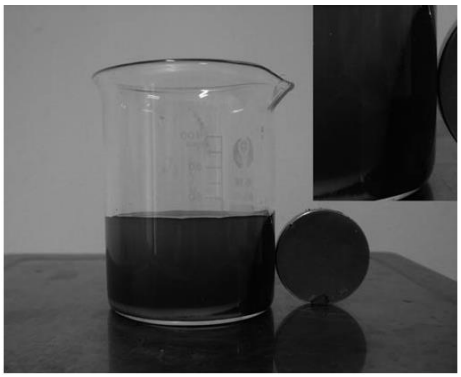

Figure 11. The separation of the Ru-Fe_3O_4–SiO_2/NH_2 sample

Conclusions

In summary, we succeeded to synthesize four Ru-based catalysts with CNT and MNP particles as carriers. The characterization of the obtained samples indicates the formation of different kind of ruthenium active phase, as a function of the preparation method and the carrier nature. Therefore, in the case of CNT-based samples, catalysts with ruthenium nanoparticles of different size and oxidation degree were identified on the external side of the CNT tubes: the higher the ruthenium concentration, the larger the nanoparticles; the larger nanoparticles, the lower the reduction degree (the higher the proportion of RuO_x). On the other hand, the MNP-based sample strictly contains cationic ruthenium species with a high degree of dispersion.

Perspectives

In agree with [12], the deposition of ruthenium on oxidized CNTs may lead to catalysts with totally different structural features and catalytic performances since: (1) the reducibility of Ru species in Ru-in-CNTs catalyst is higher than those of Ru-out-CNTs due to the electron-deficient of CNT interior surface; (2) the encapsulation of Ru particles inside the CNT channel can enhance the interaction between the reactants and catalytic sites to give higher conversion; (3) such encapsulation can also reduce the leaching of Ru particles during the reaction process, which can improve the stability of catalyst. Therefore, an important activity which will be achieved in the next research step is the oxidation of the as-received CNT, by using different oxidation methodologies. Obtained samples will be thereafter impregnated with ruthenium chloride in the view of producing Ru@CNT catalysts with different catalytic features.

The concentration of ruthenium will be established as a function of the results obtained in the synthesis of alanine with Ru/CNT samples already prepared and presented in this report. In this way, an optimization of the catalytic features will be made for the best catalytic performances in the chosen synthesis.

References

[1] – P. Serp, M. Corrias, P. Kalck, Carbon nanotubes and nanofibers in catalysis, Appl. Catal. A: General, 253 (2003) 337-358

[2] – Z. Zhong, B. Liu, L. Sun, J. Ding, J. Lin, K.L. Tan, Dispersing and coating of transition metals Co, Fe and Ni on carbon materials, Chem. Phys. Lett., 362 (2002) 135-143

[3] – P. Chen, X. Wu, J. Lin, K.L. Tan, Synthesis of Cu Nanoparticles and Microsized Fibers by Using Carbon Nanotubes as a Template, J. Phys. Chem, 103, 22 (1999) 4559-4561

[4] – S. Shylesh, V. Schunermann, W.R. Thiel, Magnetically Separable Nanocatalysts: Bridges between Homogeneous and Heterogeneous Catalysis, Anew. Chem. Int. Ed., 49 (2010) 3428-3459

[5] – E. McCafferty, J.P. Wightman, Determination of the Concentration of Surface hydroxyl Groups on Metal Oxide Films by a Quantitative XPS Method, Surf. Interface Anal. 26 (1998), 549-564

[6] – I. Podolean, V. Kuncser, N. Gheorghe, D. Macovei, V.I. Parvulescu, S.M. Coman, Ru-based magnetic nanoparticles (MNP) for succinic acid synthesis from levulinic acid, Green Chem, 2013

[7] – F.D. Schouwer, L. Claes, A. Vandekerkhove, J. Verduyckt, D. E. De Vos, Protein-rich biomass waste as a resource for future bio-refineries: state of the art, challenges and opportunities, Chem. Sus. Chem., 12 (2019) 1272-1303

[8] – W. Deng, Y. Wang, S. Zhang, K. M. Gupta, M. J. Hulsey, H. Asakura, L. Liu, Y. Han, E. M. Karp, G. T. Beckham, P. J. Dyson, J. Jiang, T. Tanaka, Y. Wang, Catalytic amino acid production from biomass derived intermediates, PNAS, 115 (2018) 5093-5098

[9] – A. Negoi, I.T. Trotus, O.M. Steiner, M. Tudorache, V. Kuncser, D. Macovei, V.I. Parvulescu, S.M. Coman, Direct Synthesis of Sorbitol and Glycerol from Cellulose over Ionic Ru/Magnetite Nanoparticles in the Absence of External Hydrogen, Chem. Sus. Chem, 6 (2013) 2090-2094

[10] – S.J. Greeg, K.S. Sing, Adsorption, Surface Area and Porosity, 1982, 957

[11] – Q.H. Yang, P.X. Hou, S. Bai, M.Z. Wang, H.M. Cheng, Adsorption and capillarity of nitrogen in aggregated multi-walled carbon nanotubes, Chem. Phys. Lett., 345 (2001) 18-24

[12] – M. Ran, Y. Liu, W. Chu, A. Borgna, Enhanced Conversion of Cellobiose to Sugar Alcohols by Controlled Dispersion of Ruthenium Nanoparticles Inside Carbon Nanotube Channels, Catal. Let, 143 (2013) 1139-1144

[13] – J. Kang, W. Deng, Q. Zhang, Y. Wang, Ru particle size effect in Ru/CNT-catalyzed Fischer-Tropsch synthesis, J. Energy Chem. , 22 (2013) 321-328

[14] – S. Thoka, C.M. Tsai, Z. Tong, A. Jena, F.M. Wang, C.C. Hsu, H. Chang, S.F. Hu, R.S. Liu, Comparative Study of Li-CO_2 and Na-CO_2 Batteries with Ru@CNT as a Cathode Catalyst, ACS Appl. Mater. Interfaces, 13 (2021) 480-490

[15] – F. Su, L. Lv, F.Y. Lee, T. Liu, A.I. Cooper, X.S. Zhao, Thermally Reduced Ruthenium Nanoparticles as a Highly Active Heterogeneous Catalyst for Hydrogenation of Monoaromatics, J. Am. Chem. Soc., 129 (2007) 14213-14223

[16] – Q. Zhang, L. Gao, J. Guo, Effects of calcination on the photocatalytic properties of nanosized TiO_2 powders prepared by $TiCl_4$ hydrolysis, Appl. Catal. B: Envir., 26 (2000) 207-215

[17] – W. Chen, Z. Fan, X. Pan, X. Bao, Effect of Confinement in Carbon Nanotubes on the Activity of Fisher-Tropsch Iron Catalyst, ACS J. Am. Chem. Soc., 130 (2008) 9414-9419

[18] – R.M.M. Abbaslou, A. Tavassoli, J. Soltan, A.K. Dalai, Iron catalyst supported on carbon nanotubes for Fischer-Tropsch synthesis: Effect of catalytic site position, Appl. Catal. A: Gen. , 367 (2009) 47-52

[19] – F. Lonyi, J. Valyon, On the interpretation of the NH_3-TPD patters of H-ZSM-5 and H-mordenite, Micropor. Mesopor. Mat., 47 (2001) 293-301

[20] – N.R. Meshram, S.G. Hedge, S.B. Kulkarni, Active sites on ZSM-5 zeolites for toluene disproportionation, Zeolites, 6 (1986) 434-438

[21] – H. Igi, N. Katana, M. Niwa, in: M. M. J. Treacy, B. K. Marcus, M. E. Bisher, J. B. Higgins (Eds.), Proceedings of the 12th International Zeolite Conference, Materials Research Society, Warrendale, PA, 1999, 2643

[22] – C.F. Wang, X.L. Pan, X.H. Bao, Direct production of light olefins from syngas over a carbon nanotube confined iron catalyst, Chem. Phys. Lett., 55 (2010) 1117-1119

[23] – J.T. Miller, B.L. Meyers, F.S. Modica, G.S. Lane, M. Vaarkamp, D.C. Koningsberger, Hydrogen Temperature-Programmed Desorption (H_2 TPD) of Supported Platinum Catalysts, J. Catal., 143 (1993) 395-408

[24] – G. Vidali, Potentials of physical adsorption, Surface Science Reports, 12 (1991) 133-181

[25] – K. Masenelli-Varlot, E. McRae, N. Dupont-Pavlovsky, Comparative adsorption of simple molecules on carbon nanotubes. Dependence of the adsorption properties on the nanotube morphology, Appl. Surf. Sci., 196 (2002) 209-215

[26] – T. Szilagyi, Fourier-Transform Infrared Study of Weak Adsorption of hydrogen on Pt/SiO_2, J. Catal., 121 (1990) 223-227

[27] – J. Chen, M.A. Hamon, H. Hu, Y. Chen, A.M. Rao, P.C. Eklund, R.C. Haddon, Solution Properties of Single-Walled Carbon Nanotubes, Science, 282, 95 (1998) 95-98

[28] – M.E. Lipinska, S.L.H. Rebelo, M.F.R. Pereira, J.A.N.F. Gomes, C. Freire, J.L. Figueiredo, New insights into the functionalization of multi-walled carbon nanotubes with aniline derivatives, Carbon, 50 (2012) 3280-3294

[29] – M. Yamaura, R.L. Camilo, L.C. Sampaio, M.A. Macedo, M. Nakamura, H.E. Toma, Preparation and characterization of (3-aminopropyl) triethoxysilane-coated magnetite nanoparticles, J. Magn. Magn. Mater., 279 (2004) 210-217

[30] – M.P. Morales, S.V. Verdaguer, M.I. Montero, C.J. Serna, Surface and Internal Spin Canting in γ-Fe_2O_3 Nanoparticles, Chem. Mater, 11 (1999) 3058-3064

[31] – M. Ma, Y. Zhang, W. Yu, H. Shen, H. Zhang, N. Gu, Preparation and characterization of magnetite nanoparticles coated by amino silane, Colloids and Surfaces A: Physicochem. Eng. Aspects, 212 (2003) 219-226

[32] – L.D. White, C.P. Tripp, Reaction of (3-aminopropyl)dimethylethoxyxilane with Amine Catalysts on Silica Surfaces, J. Colloid Interface Sci., 232 (2000) 400-407

Annex 1. Thermogravimetric analysis of CNT carrier

In order to establish the optimum temperature for the calcination of samples 1%Ru/CNT, 3%Ru/CNT and 5%Ru/CNT the TG analysis of CNT was previously performed. According to the TGA profile in the air atmosphere (Figure 1), the mass loss of the CNT starts slowly in the temperature range 440-460 ℃. However, after 500°C the CNT begins to be fast oxidized (a process possible catalysed by the transition metals remained into the material from the synthesis of CNT) and the mass of the sample quickly declines with the increase of temperature. Bearing in mind this, the calcination step of the Ru-based catalysts was performed at 350°C in order to avoid the decomposition of the support.

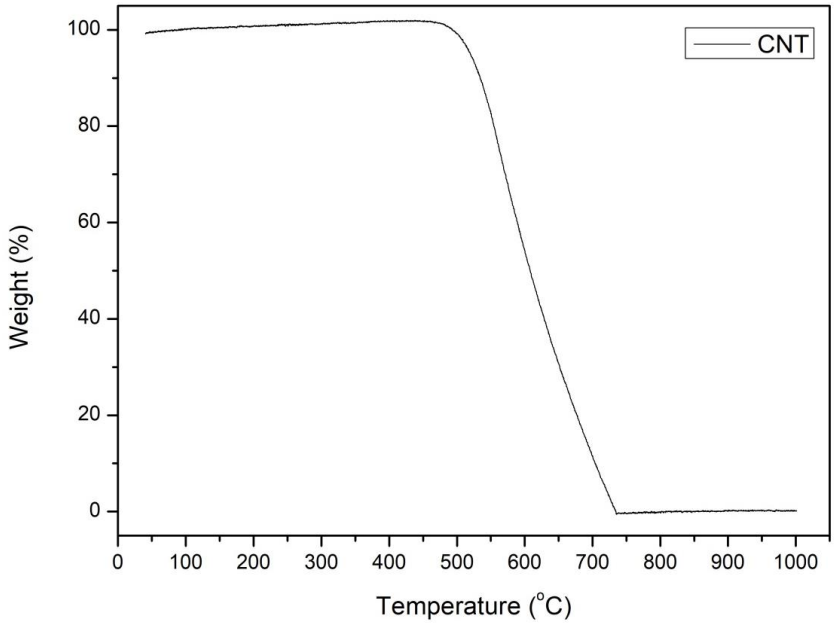

Figure 1. TGA profile in air atmosphere for as-received CNT